Practical Terminal Sliding Mode Control of Active Power Filters by Self-Organizing Hermite Fuzzy Neural Network

Shixi Hou, Jienan Han, Yundi Chu, Cheng Zhou, and Juntao Fei, *Senior Member, IEEE*

***Abstract*—To mitigate harmonic contamination, this article introduces a supertwisting practical terminal sliding mode controller (STPTSMC) using a self-organizing Hermite fuzzy neural network (SOHFNN) for an active power filter (APF) with unknown model nonlinearities. First, a practical terminal sliding mode because of its benefits in offering a continuous and nonsingular characteristic is adopted, and a supertwisting sliding mode control algorithm is embedded to smoothen chattering control signals and enhance APF's dynamic tracking capability. Second, the fusion of fuzzy neural network, self-organizing mechanism, feature selection algorithm, and Hermite activation function empowers the SOHFNN to precisely estimate the uncertain STPTSMC owing to component parameter perturbation of APF. Finally, the feasibility and efficacy of the SOHFNN-STPTSMC scheme have been validated through simulation and experimental efforts, evidencing its improvement performance relative to other methodologies.**

***Index Terms*—Fuzzy neural network (FNN), Hermite orthogonal polynomials, practical terminal sliding mode (PTSM) controller, self-organizing mechanism.**

I. Introduction

AGAINST the backdrop of burgeoning advancements in power electronic technology and the proliferation of distributed generations, the power system is increasingly burdened with a significant influx of harmonics, posing a severe risk to its safe and stable functioning [1], [2]. Therefore, addressing and mitigating these harmonics is of utmost importance. Active power filter (APF), known for its excellent harmonic compensation capabilities, has emerged as a prominent solution for harmonics mitigation [3], [4], [5]. The existing APF topology mainly includes buck-boost type and full-bridge type [6], [7], [8]. Compared with the simplified buck-boost topology, the full-bridge structure offers higher degrees of freedom for control and a wider compensation bandwidth, which is more suitable for the increasing complexity of harmonics. Thus, APF with full-bridge topology is considered as research objective in this article. Nonetheless, the escalating complexity of harmonic pollution alongside heightened demands for power quality challenges the efficacy of conventional control strategies for APF, such as PI and hysteresis control. As a result, the development of current tracking strategies, integrating the advantages of diverse control techniques, emerges as a pivotal research focus.

Sliding mode control (SMC) [9], [10], [11], [12], [13], [14], [15], [16] is widely acknowledged as a robust control approach, capable of addressing uncertainties and external disturbances effectively. Among them, terminal sliding mode control (TSMC) [12], [13], [14] emerges as an enhancement over traditional SMC, offering finite-time convergence and enhanced robustness. However, TSMC faces challenges such as potential singularity and persistent chattering in practical implementations. The research detailed in [15] unveils a pioneering sliding surface design via the practical TSMC (PTSMC) manifold, employing a hyperbolic tangent function intertwined with a terminal attractor. This PTSMC is characterized by a Lipschitz-continuous property and possesses a notably steep gradient for the generalized velocity at its origin, which effectively eliminates the necessity for manifold switching to address the singularity issues associated with TSMC, maintaining efficacy even when controlled states are proximal to the equilibrium. Additionally, owing to its capabilities in diminishing chattering, super-twisting sliding mode control (STSMC) [17], [18], [19] has found application across numerous studies. Therefore, supertwisting practical terminal sliding mode controller (STPTSMC) is exploited APF in this article. However, STPTSMC technology fundamentally relies on detailed information of nonlinear systems, which poses a significant challenge in real-world applications. Consequently, there is a need to develop an enhanced STPTSMC approach for APF with indeterminate parameters.

The integration of SMC with diverse observers [20], [21], [22], [23], [24] or neural networks (NNs) [25], [26], [27], [28], [29], [30] has garnered significant attention in recent scholarly investigations. The profound computational capabilities of NNs, theoretically enable them to approximate any nonlinear function. Within numerous NNs, hidden neurons traditionally utilize sigmoid or Gaussian functions as their activation mechanism. However, there has been no conclusive evidence to suggest

Received 10 April 2025; revised 17 July 2025; accepted 20 August 2025. Date of publication 28 August 2025; date of current version 22 October 2025. This work was supported in part by the National Natural Science Foundation of China under Grant 62103132 and Grant 62003132, in part by the Natural Science Foundation of Jiangsu Province under Grant BK20241779, and in part by the Major Special Science and Technology Project of Yunnan Province under Grant 202402AF080006. Recommended for publication by Associate Editor H. S. Krishnamoorthy. *(Corresponding author: Shixi Hou.)*

The authors are with the College of Artificial Intelligence and Automation and Jiangsu Key Laboratory of Power Transmission and Distribution Equipment Technology, Hohai University, Nanjing 210098, China (e-mail: houshixi@hhu.edu.cn; 1962510103@hhu.edu.cn; 20191011@hhu.edu.cn; 221620010066@hhu.edu.cn; johnfei123@163.com).

Color versions of one or more figures in this article are available at https://doi.org/10.1109/TPEL.2025.3603892.

Digital Object Identifier 10.1109/TPEL.2025.3603892

that uniform application of a single activation function across all hidden neurons can optimize generalization capabilities. Ma and Khorasani [31] introduce the concept of employing Hermite orthogonal polynomials for the activation of hidden neurons. This approach, as evidenced through various test scenarios, offers a more effective search domain and superior functional performance in comparison to traditional sigmoid or Gaussian activations. Moreover, unlike the Gaussian function, utilizing Hermite orthogonal polynomials eliminates the necessity for offline determination of activation function parameters, thereby circumventing potential detriments due to inappropriate parameter.

In addressing the intricacies of dynamic systems, the adoption of a fuzzy neural network (FNN) strategy proves instrumental. This approach leverages the synergistic integration of fuzzy control's expert knowledge and the robust approximation capabilities of NNs to estimate indistinct dynamic models effectively. Consequently, this has precipitated a considerable volume of research endeavors employing FNN to approximate dynamic systems [32], [33], [34], [35], [36]. While FNN has always treated all inputs equally important, new research indicates that some inputs are not as important as others. Highlighting the significance of distinguishing and extracting pivotal input features, there is a compelling argument for the creation of an effective feature selection (FS) strategy to enhance network efficiency [37], [38]. Moreover, in pursuit of optimizing FNN's fuzzy reasoning capabilities, some researchers have introduced a novel compensatory fuzzy neural network (CFNN) architecture. Evidence suggests this CFNN framework significantly boosts the FNN's learning velocity [38], [39]. The structure of FNNs in deterministic systems frequently depends on empirical data to ascertain the required fuzzy rules. In order to reduce this reliance, a self-organizing fuzzy neural network (SOFNN) was developed. This novel method guarantees that FNN runs steadily and effectively with only an initial suitable set of fuzzy rules by enabling SOFNN to dynamically modify its fuzzy rules based on a set learning mechanism [40], [41], [42].

Based on the above discussion, we still need to address the following issues.

1) The existing TSMC faces challenges including potential singularity and persistent chattering in practical implementations.
2) The existing activation functions for NNs often need impose the restrictions on the range of input data, which may distort the distribution of original data, thus leading to the loss of key features.
3) When dealing with complex time-varying systems, the existing NNs struggle to distinguish between key information and redundant noise, resulting in weak antidisturbance performance.
4) The characteristic of fixed structure in the existing NNs significantly restricts their adaptability to dynamic changes in the operating environment.

Therefore, this article introduces an STPTSMC for APF to achieve harmonic current compensation, utilizing a self-organizing Hermite neural network (SOHFNN). In addition to Section I, Section II briefly outlines the APF principle and designs the STPTSMC. Section III details the SOHFNN structure and its self-organizing mechanism. The proposed control algorithm is discussed in Section IV. Sections V and VI validate the method's effectiveness through simulation and hardware experiments, respectively. Finally, Section VII concludes the article.

Remark 1: By contrasting with prior research, the contributions and unique features of this article can be more prominently emphasized.

1) Compared with TSMC in [43] and [44], the developed STPTSMC applies the hyperbolic tangent function and supertwisting technology to solve the singularity problem and chattering phenomenon, simultaneously, which effectively enhances the control performance of nonlinear systems.
2) Compared with Gaussian activation function in [45], the exploited activation function using Hermite polynomials can achieve a more efficient search space, leverage the full information of input data, and enable the proposed SOHFNN to perform more effectively in complex system.
3) Against other FNNs with simple fuzzy reasoning in [46], the SOHFNN utilizes the FS technology to focus on highly correlated information while ignore irrelevant one, thus effectively enhancing its antiinterference capabilities.
4) Compared with other fixed-structure FNNs in [47] and [48] the proposed SOHFNN that incorporates a self-organizing mechanism enables the dynamic addition and removal of neurons according to task requirements, thereby continuously maintaining high-precision modeling capabilities.

Remark 2: Although traditional PI/PR controllers can be used to control the full bridge, they possess the following key limitations: difficulty in handle parameter perturbations and external disturbances, lack of finite-time convergence capability, and high reliance on model accuracy, leading to unsatisfactory response against dynamic changes. To address the limitations of conventional PI/PR control, the STPTSMC with SOHFNN is developed in this article.

II. Problem Formulation

The circuit topology of a single-phase APF is depicted in Fig. 1. The symbols U_s, $U_{\rm dc}$, i_c, i_L, R, L, and C stand for source voltage, dc-link capacitor voltage, compensation current, load current, equivalent resistance, inductor, and dc-link capacitor, respectively. In the field of APF current regulation, a critical challenge is devising a control approach that significantly reduces the error between the target command current i_c^* and the measured compensation current i_c.

The internal current loop of the APF is characterized dynamically by the following description:

$$\ddot{i}_c = \frac{R^2}{L^2} i_c - \frac{R}{L^2} U_s + \frac{1}{L}\dot{U}_s + \left(\frac{R}{L^2} U_{\rm dc} - \frac{1}{L}\dot{U}_{\rm dc}\right) u + H(t, i_c). \tag{1}$$

In (1), $H(t, i_c) = -\frac{R}{L} H_m - \frac{U_{dc}}{L}\dot{u} + \dot{H}_m$ represents the lumped uncertainties, where $H_m =$

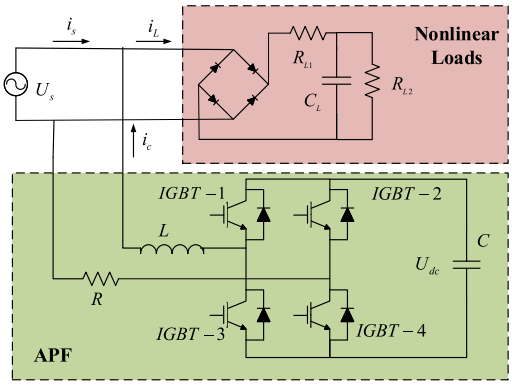

Fig. 1. Circuit diagram of APF.

$\frac{(R\Delta L - L\Delta R)i_c - U_s\Delta L + uU_{\rm dc}\Delta L}{L(L+\Delta L)} + h$, ΔL and ΔR denote as the parameter variation, and u represents switching state. In practical systems, it is a common assumption that the uncertainties including external disruptions from load and grid interactions alongside internal variations due to aging and temperature fluctuations of power components can be represented as a lumped term [49], [50].

Then, the single-phase APF model is simply derived as

$$\ddot{i}_c = f(i_c) + U + H(t, i_c) \tag{2}$$

where $f(i_c) = \frac{R^2}{L^2} i_c - \frac{R}{L^2} U_s + \frac{1}{L}\dot{U}_s$,$U = (\frac{R}{L^2} U_{\rm dc} - \frac{1}{L}\dot{U}_{\rm dc})u$.

Assumption 1: $H(t, i_c)$ is assumed to be a continuous bounded function, and H_1 represents the upper bound of $H(t, i_c)$.

Defining the tracking error, along with its derivative, in the subsequent manner:

$$e = i_c - i_c^* \tag{3}$$

$$\dot{e} = \dot{i}_c - \dot{i}_c^* \tag{4}$$

where $\dot{i}_c^*$ is the reference compensation current.

And the derivative of $\dot{e}$ can be derived as

$$\ddot{e} = \ddot{i}_c - \ddot{i}_c^*. \tag{5}$$

Traditional SMC typically employs a linear simple sliding surface that does not guarantee finite-time convergence of the state variable to the equilibrium state. While, the STPTSMC incorporates a supertwisting algorithm to rapidly stabilize the system's states within a predefined compact set around the equilibrium, enhancing precision and reducing chattering. The formulation of the STPTSM surface can be expressed as follows:

$$s = \mu e^{1-q/p} \tanh(k e^{q/p}) + \dot{e} \tag{6}$$

where $p, q \in R^+$, $\mu, k \in R^+$,and $p > q$.

Taking derivative of (6) yields

$$\dot{s} = \mu \left\{ (1 - q/p) \tanh(k e^{q/p}) \, / e^{q/p} + kq/p \left[1 - \tanh^2(k e^{q/p}) \right] \right\} \dot{e} + \ddot{e}. \tag{7}$$

The control laws are formulated as follows:

$$u_{\rm STPTSMC} = u_{\rm eq} + u_{\rm sw}. \tag{8}$$

Using (2) and (5), and disregarding the disturbance $H(t, i_c)$, while setting $\dot{s} = 0$, the equivalent controller $u_{\rm eq}$ can be expressed as

$$u_{eq} = \ddot{i}_c - f(x) - \mu \left\{ \left\{ (1 - q/p) \tanh(k e^{q/p}) \, / e^{q/p} + kq/p \left[1 - \tanh^2(k e^{q/p}) \right] \right\} \dot{e}. \tag{9}$$

The supertwisting switching controller is denoted as

$$u_{sw} = -k_1 \sqrt{|s|} \mathrm{sgn}(s) - \int k_2 \mathrm{sgn}(s) dt \tag{10}$$

where $k_1, k_2 > 0$. It is assumed that $|H(t, i_c)| \le H_1 < k_1$,$|\dot{H}(t, i_c)| \le H_2 < k_2$, and H_2 is the upper bound of $\dot{H}(t, i_c)$.

Theorem 1: Under the framework of the nonlinear APF model (2) and employing the controller specified in (8), the finite-time stability of the closed-loop system is ensured.

Proof: The Lyapunov candidate is $V_1 = \frac{1}{2} s^2$. Upon substitution of (7) and the ideal controller (8) into the derivative of the Lyapunov function V_1, we derive

$$\begin{aligned} \dot{V}_1 &= s\dot{s} \\ &= s[H(t, i_c) - k_1 \sqrt{|s|} \mathrm{sgn}(s) - \int k_2 \mathrm{sgn}(s) dt)] \\ &= sH(t, i_c) - k_1 |s| \sqrt{|s|} - s \int k_2 \mathrm{sgn}(s) dt \\ &\le |s| \, |H(t, i_c)| - k_1 |s| \sqrt{|s|} - |s| \int k_2 dt \\ &= |s| \left| \int \dot{H}(t, i_c) dt \right| - k_1 |s| \sqrt{|s|} - |s| \int k_2 dt. \end{aligned} \tag{11}$$

As $H(t, i_c) = \int \dot{H}(t, i_c) dt$ and $|\int \dot{H}(t, i_c) dt| \le \int |\dot{H}(t, i_c)| dt$

$$\dot{V}_1 \le |s| \int \left| \dot{H}(t, i_c) \right| dt - k_1 |s| \sqrt{|s|} - |s| \int k_2 dt. \tag{12}$$

Because $k_2 > H_2 > |\dot{H}(t, i_c)|$, then

$$\begin{aligned} \dot{V}_1 &\le |s| \int H_2 dt - k_1 |s| \sqrt{|s|} - |s| \int k_2 dt \\ &= -|s| \left(\int k_2 dt - \int H_2 dt \right) - k_1 |s| \sqrt{|s|} \\ &\le -k_1 |s| \sqrt{|s|} \le 0 \end{aligned} \tag{13}$$

$$\dot{V}_1 \le -k_1 (|s|)^{\frac{3}{2}} = -2^{\frac{3}{4}} \cdot k_1 \cdot V^{\frac{3}{4}}. \tag{14}$$

Equation (14) can alternatively be expressed as

$$\frac{dV_1}{V_1^{\frac{3}{4}}} \le -2^{\frac{3}{4}} \cdot k_1 \cdot dt. \tag{15}$$

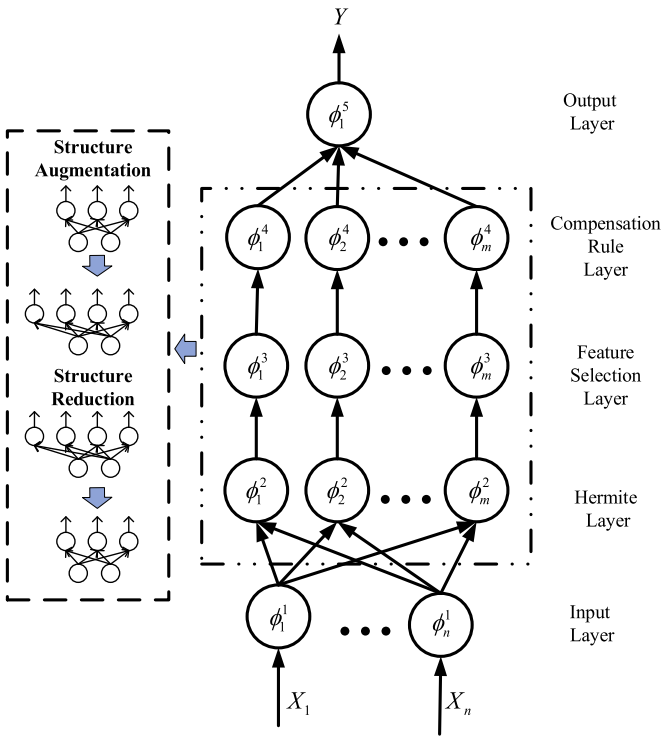

Fig. 2. Structure of SOHFNN.

Presuming stability of the system at $t = t_r$, (15) is integrated with respect to time

$$\int_{V(0)}^{V(t_r)} \frac{dV_1}{V_1^{\frac{3}{4}}} \leq -2^{\frac{3}{4}} \int_0^{t_r} k_1 dt. \tag{16}$$

From (16), the range of t_r is determined as

$$t_r \leq -\frac{4 \cdot (V_1(t_r)^{\frac{1}{4}} - V_1(0)^{\frac{1}{4}})}{2^{\frac{3}{4}} \cdot k_1}. \tag{17}$$

This also substantiates the notion that employing controller (8) ensures the system's stability within a finite duration.

Despite the controller (8) necessitating precise model parameters of APF, which are frequently uncertain in real-world scenarios, this article introduces an innovative solution through the deployment of an SOHFNN approximator. This approach effectively circumvents the aforementioned limitations by employing SOHFNN to replicate the original controller, as elaborated in Section III, thereby significantly improving control efficacy.

III. Self-Organizing Hermite Fuzzy Neural Network

This section describes the architecture of the SOHFNN, which uses Hermite orthogonal polynomials as the activation function, and details the self-organizing mechanism governing the network nodes' evolution.

A. Structure of SOHFNN

As depicted in Fig. 2, the SOHFNN framework is organized into five layers: the input layer; Hermite layer; FS layer; compensation rule layer; and output layer. When the network input is represented as $X(t) = [X_1(t), X_2(t), \ldots, X_n(t)]$ and the output as $Y(t)$, the formulation of each layer can be derived as follows.

a) Input Layer: Primarily, it serves the purpose of receiving the input signal $X(t) = [X_1(t), X_2(t), \ldots, X_n(t)]$. In this layer, there exist n nodes, with each node corresponding to a formal parameter of $f(i_c)$. The inputs $\theta_i^1(t)$ and outputs $\phi_i^1(t)$ of each node can be defined as

$$\begin{cases} \theta_i^1(t) = X_i(t) \\ \phi_i^1(t) = \theta_i^1(t) \end{cases}$$
$$i = 1, 2, \ldots, n \tag{18}$$

where $X_i(t)$ represents the input of *i*th formal parameter of $f(i_c)$ at time *t*.

b) Hermite Layer: In this layer, there exist *m* nodes, with each node having *n* inputs and one output. The inputs $\theta_j^2(t)$ and outputs $\phi_j^2(t)$ of each node in this layer are defined as

$$\begin{cases} \theta_j^2(t) = \Theta \\ \phi_j^2(t) = \frac{1}{\sqrt{2^j j! \sqrt{\pi}}} e^{-\theta_j^2(t)/2} H_j(\theta_j^2(t)) \quad j = 1, 2, \ldots, m \end{cases} \tag{19}$$

where $\Theta = [\phi_1^1, \phi_2^1, \ldots \phi_n^1]$ is input vector formed by all inputs of Hermite layer. The Hermite orthogonal polynomials are recursively defined as follows:

$$\begin{aligned} &H_0(r) = 1 \\ &H_1(r) = 2r \\ &\vdots \\ &H_l(r) = 2rH_{l-1}(r) - 2(l-1)H_{l-2}(r), \text{for } l \geq 2 \end{aligned} \tag{20}$$

where *r* represents a vector.

c) Feature Selection Layer: In this layer, *m* nodes are present, each directly aligning with a node in the Hermite layer. These nodes are tasked with evaluating the feature degree based on the outputs from the Hermite Layer. The definitions of inputs and outputs for every node within this layer are established as

$$\begin{cases} \theta_j^3(t) = (1 - \exp(-\rho_j^2(t)))\mathrm{e}^{\phi_j^2(t)} \\ \phi_j^3(t) = \begin{cases} \theta_j^3(t) & f_d(\rho_j(t)) \geq T(t) \\ 0 & f_d(\rho_j(t)) < T(t) \end{cases} \end{cases}$$
$$f_d(\rho_j(t)) = 1 - \exp(-\rho_j^2(t)); j = 1, 2, \ldots, m \tag{21}$$

where $f_d(\rho_j(t)) \in [0, 1)$ denotes the feature degree associated with *j*th node, ρ_j is identified as the feature degree factor for $f_d(\rho_j(t))$, and the initial value of $\rho_j(0)$ typically established at 1. $T(t)$ is designated as the threshold function for the characteristic degree, which is defined as

$$T(t) = \frac{1}{m[1 + (1 + e^2 + \dot{e}^2)] + a_T} \tag{22}$$

where $a_T > 0 \in R$ is threshold function regulator.

To quantify the impact of individual nodes on the ultimate output, a metric termed as the importance index is established

$$\eta_j(t) = \begin{cases} 1 & f_d(\rho_j(t)) \geq T_j(t) \\ \eta_j(t-1)\exp(-\chi) & f_d(\rho_j(t)) < T_j(t) \end{cases} \tag{23}$$

where $\eta_j(t-1)$ represents the importance of $\eta_j(t)$ at the last moment, and $\chi > 0 \in R$ is a preset constant.

The operation of the FS algorithm is delineated as follows: When $f_d(\rho_j(t))$attains a value of 1, it implies that $\phi_j^3(t)$ is equivalent to $\phi_j^2(t)$, indicating the substantial value of the feature information possessed by the *j*th node, necessitating its complete transfer to the subsequent layer. Should $f_d(\rho_j(t))$lie within the range of $T(t)$ and 1, it suggests that the feature information from the *j*-th node possesses moderate utility. Under such circumstances, $\phi_j^2(t)$,adjusted by the feature degree $T(t)$, is advised to be conveyed in part to the following layer. Conversely, if $f_d(\rho_j(t))$ is less than or equal to $T(t)$, it is inferred that the feature information of the *j*th node is considered to be of minimal benefit, leading to the decision not to forward $\phi_j^2(t)$ to the next layer. The transfer of output from the Hermite layer to the subsequent layer is conducted on a selective basis, fully, partially, or not, based on the evaluated significance of the feature information.

d) Compensation Rule Layer: This layer comprises m nodes, each aligning with a corresponding node in the FS layer. The inputs and outputs for each node are specified as follows:

$$\begin{cases} \theta_j^4(t) = (\phi_j^3(t))^{1-\lambda_j(t)+\lambda_j(t)/n} \\ \phi_j^4(t) = \frac{\theta_j^4(t)}{\sum_{i=1}^m \theta_i^4(t)} \end{cases} \quad j = 1, 2, \ldots, m \tag{24}$$

where $\lambda_j(t)$ is defined as a function for compensation degree, devised to dynamically refine the structure of the SOHFNN, as specified

$$\lambda_j(t) = \frac{\alpha_j^2(t)}{\alpha_j^2(t) + \beta_j^2(t)}, \alpha_j, \beta_j \in R \tag{25}$$

where $\alpha_j$and β_j are the corresponding compensatory factor parameters of $\lambda_j(t)$.

To enhance the network's generalization capabilities, this article incorporates a compensation layer. As detailed in (24), the inclusion of a compensation rule layer adds an extra dimension of flexibility to NNs, indicating that the outputs from this layer are shaped not solely by the inputs but are also modulated by a compensation degree. Traditionally, FNNs assign the role of this layer to what is known as the rule layer. It is important to note that setting the compensation degree $\lambda_j(t)$ to zero results in the output of the SOHFNN's compensation layer mirroring that of the conventional FNN's rule layer. Consequently, the compensation layer presented in this research effectively subsumes the conventional rule layer, treating it as a particular instance.

e) Output Layer: This layer contains a single node, designated to approximate the output of $f(i_c)$. The definitions of the inputs and the output for this node are outlined as follows:

$$\begin{cases} \theta_j^5(t) = \phi_j^4(t) \\ \phi_1^5(t) = \Psi^T W \end{cases} \quad j = 1, 2, \ldots, m \tag{26}$$

where $\Psi = [\theta_1^5 \quad \theta_2^5 \quad \cdots \quad \theta_m^5]^T \in R^{m\times 1}$ is input vector formed by all inputs of output layer, and $W = [w_1(t) \quad w_2(t) \quad \cdots \quad w_m(t)]^T \in R^{m\times 1}$ represents weight vector matched with Ψ. Therefore, we can obtain the output $Y(t) = \phi_1^5(t)$ of the SOHFNN.

The configuration of a conventional FNN is largely reliant on empirical insights. To minimize reliance on pre-existing knowledge, the SOHFNN employs a self-learning approach. This strategy is bifurcated into two main policies: structure augmentation and structure reduction, each of which will be discussed in separate subsections.

B. Structure Augmentation Policy

The policy for adding structure is governed by three specific criteria, and the SOHFNN will proceed with the addition of structure only upon the fulfillment of all these conditions. The particulars are outlined as follows.

1) *Error Constrain.* For system error e_1 and a predefined threshold T_{a_1}:If $|e| > T_{a\_1}$, this suggests that the SOHFNN's approximation capabilities are inadequate, necessitating an expansion of its structure. Conversely, if $|e| \leq T_{a\_1}$, the SOHFNN is deemed to possess sufficient approximation precision, and thus, no expansion of its structure is required at this juncture.
2) *Feature Degree Constrain.* For the highest feature degree, represented as $\rho_{\max} = \max\{1 - \exp(-\rho_j^2)\}, j = 1, 2, \ldots, m$and a threshold T_{a_2}: When $\rho_{\max} \leq T_{a\_2}$ it reflects a low Hermite layer response of the SOHFNN to the current input, suggesting potential underfitting. This indicates a lack of network capacity to fully capture and adapt to the input's complexities, warranting a structural enhancement of the SOHFNN. If $\rho_{\max} > T_{a\_2}$, it demonstrates that the network is sufficiently complex to address the intricacies of the input effectively, negating the need for structural addition. The essence of the feature degree constraint is to ensure structure augmentation aligns with the necessity, promoting efficiency and precision in response to input dynamics.
3) C*alculation Burden Constraint.* Given the computational limits of actual control devices, this constraint considers the computational load with the aim of limiting node expansion in each layer. For the SOHFNN, to avert excessive computational demands, the maximal allowable structure expansion is set at T_{a_3}. Structure addition is contemplated only when the current number of structures $m < T_{a\_3}$.

Hence, it can be asserted that the structure of SOHFNN expands when the following conditions are concurrently met: $|e| > T_{a\_1}, \rho_{\max} \leq T_{a\_2}$ and $m < T_{a\_3}$. This expansion denotes an augmentation in the node count across the three intermediary layers of the network, with the initialization parameters for these additional nodes being established by (27). Subsequent to this, parameter updates are carried out in accordance with

the designated update mechanism. In scenarios where these conditions are not fulfilled, the SOHFNN confines its operations to adjustments of parameters within its pre-existing framework

$$\begin{cases} \rho_{m+1}(t) = 1 \\ \eta_{m+1}(t) = 1 \\ \alpha_{m+1}(t) = \beta_{m+1}(t) = 1 \\ w_{m+1}(t) = 1 \end{cases}. \tag{27}$$

C. Structure Reduction Policy

The expansion of SOHFNN's structure not only enhances its capabilities, but also elevates the computational load. To manage the maximum configuration of SOHFNN effectively, it is desirable to employ structural pruning. This approach aims to alleviate the computational demands by excising components that offer minimal contribution to the functionality of SOHFNN. The pruning strategy is governed by three specific criteria, delineated as follows.

1) *Error Index Constraint:* For the pruning index expressed as $1 + e^2 + \dot{e}^2$ and a pruning threshold denoted by T_{d_1}, structural pruning is considered only when $1 + e^2 + \dot{e}^2 > T_{d\_1}$. This approach is adopted because a cumulative error $1 + e^2 + \dot{e}^2$ that is more than or equal to T_{d_1} increases the threshold for the feature layer, potentially causing certain structures within the SOHFNN to become temporarily ineffective. To prevent unnecessary pruning operations, no pruning will be conducted under these circumstances.
2) *Importance Constraint:* The Importance Constraint involves assessing the importance index, denoted as $\eta_j(t)$, against a specified threshold T_{d_2}. If $\eta_j(t) \leq T_{d\_2}$, it suggests that a segment of the SOHFNN's structure has remained inactive over an extended period, warranting its removal to eliminate superfluous computations.
3) *Calculation Burden Constraint:* In the case of SOHFNN, implementing structural pruning is acknowledged to diminish the computational load. However, it is desirable for SOHFNN to maintain a certain level of structural redundancy to effectively manage unpredictable disturbances. As such, the baseline quantity of structures within SOHFNN is established at T_{d_3}, with structural pruning being contemplated only when $m > T_{d\_3}$.

Hence, the following criterion is established: structural pruning is initiated when the conditions $1 + e^2 + \dot{e}^2 > T_{d\_1}, \eta_j(t) \leq T_{d\_2}$ and $m > T_{d\_3}$ are concurrently satisfied. In scenarios where these conditions do not align, the SOHFNN's architecture is refined through parameter adjustment.

This section provides an in-depth exploration of SOHFNN, with the subsequent part examining the applications to STPTSMC that are based on SOHFNN.

IV. Proposed Control Algorithm

For real-world APF systems, accurately modeling the system becomes challenging due to component parameter perturbations and various external influences, the above STPTSMC approach in (8) is difficult for engineering reality. To mitigate reliance on precise prior knowledge for the STPTSMC, boost its robustness and enhance control effectiveness, the output from the SOHFNN is leveraged to approximate the controller u_{STPTSMC}. Additionally, a robust compensator, denoted as u_{rob}, is integrated into the control architecture to address other uncertainties, including approximation inaccuracies.

The control strategy introduced in this article is designed as

$$U = u_{\text{SOHFNN}} + u_{\text{rob}}. \tag{28}$$

Assumption 2: There is an ideal SOHFNN to approximate the controller u_{STPTSMC}, such that $u^*_{\text{SOHFNN}} = \Psi^{*T} W^* + \varepsilon$, where ε presents reconstruction error satisfying $|\varepsilon| \leq \varepsilon_b$, and ε_b represents the maximum allowable reconstruction error, $\Psi^* = \Psi^*(X(t), \rho^*, \alpha^*, \beta^*)$, W^*, ρ^*, α^*, β^* are ideal parameters of ideal SOHFNN.

The actual output of SOHFNN can be given as

$$\hat{u}_{\text{SOHFNN}} = \hat{\Psi}^T(X(t), \hat{\rho}, \hat{\alpha}, \hat{\beta})\hat{W} \tag{29}$$

where $\hat{\rho}$, $\hat{\alpha}$, $\hat{\beta}$, $\hat{W}$ are the estimated values of ρ^*, α^*, β^*, W^*.

Combining Taylor's formula expansion, the approximation error of u_{SOHFNN} can be expressed as

$$\begin{aligned} \tilde{u} &= u^*_{\text{SOHFNN}} - \hat{u}_{\text{SOHFNN}} \\ &= \Psi^{*T} W^* + \varepsilon - \hat{\Psi}^T \hat{W} \\ &= (\hat{\Psi}^T + \tilde{\Psi}^T)(\hat{W} + \tilde{W}) - \hat{\Psi}^T \hat{W} + \varepsilon \\ &= \hat{\Psi}^T \tilde{W} + \left(\frac{\partial \hat{\Psi}^T}{\partial \rho}\bigg|_{\rho=\hat{\rho}} \tilde{\rho} + \frac{\partial \hat{\Psi}^T}{\partial \alpha}\bigg|_{\alpha=\hat{\alpha}} \tilde{\alpha} \right. \\ &\quad \left. + \frac{\partial \hat{\Psi}^T}{\partial \beta}\bigg|_{\beta=\hat{\beta}} \tilde{\beta} + o_{b\hat{\Psi}^T} \right) \hat{W} + \tilde{\Psi}^T \tilde{W} + \varepsilon \\ &= \hat{\Psi}^T \tilde{W} + \left(\frac{\partial \hat{\Psi}^T}{\partial \rho}\bigg|_{\rho=\hat{\rho}} \tilde{\rho} + \frac{\partial \hat{\Psi}^T}{\partial \alpha}\bigg|_{\alpha=\hat{\alpha}} \tilde{\alpha} \right. \\ &\quad \left. + \frac{\partial \hat{\Psi}^T}{\partial \beta}\bigg|_{\beta=\hat{\beta}} \tilde{\beta} \right) \hat{W} + o_b \end{aligned} \tag{30}$$

$$o_b = o_{b\hat{\Psi}^T} \hat{W} + \tilde{\Psi}^T \tilde{W} + \varepsilon \tag{31}$$

where $\tilde{W} = W^* - \hat{W}$, $\tilde{\rho} = \rho^* - \tilde{\rho}$, $\tilde{\alpha} = \alpha^* - \hat{\alpha}$, $\tilde{\beta} = \beta^* - \hat{\beta}$, $o_{b\hat{\Psi}^T}$ is the high-order term of Taylor's formula expansion at Ψ^{*T} for $\hat{\Psi}^T$, o_b represents the sum of the approximation errors and assumption $|o_b| \leq o^*_{b\max}$.

Theorem 2: For APF system (2) and practical terminal sliding surface (6), when the adaptive parameter update law of the SOHFNN is designed as (32)–(36), and the robust controller u_{rob} is designed as (37), the stability of APF system is assured

$$\dot{\hat{\rho}} = -\dot{\tilde{\rho}} = -\eta_1 s \frac{\partial \hat{\Psi}^T}{\partial \rho}\big|_{\rho=\hat{\rho}} \hat{W} \tag{32}$$

$$\dot{\hat{\alpha}} = -\dot{\tilde{\alpha}} = -\eta_2 s \frac{\partial \hat{\Psi}^T}{\partial \alpha}\big|_{\alpha=\hat{\alpha}} \hat{W} \tag{33}$$

$$\dot{\hat{\beta}} = -\dot{\tilde{\beta}} = -\eta_3 s \frac{\partial \hat{\Psi}^T}{\partial \beta}\bigg|_{\beta=\hat{\beta}} \hat{W} \tag{34}$$

$$\dot{\hat{W}} = -\dot{\tilde{W}} = -\eta_4 s \hat{\Psi}^T \tag{35}$$

$$\dot{\hat{o}}_{b\max} = -\dot{\tilde{o}}_{b\max} = \eta_5 |s| \tag{36}$$

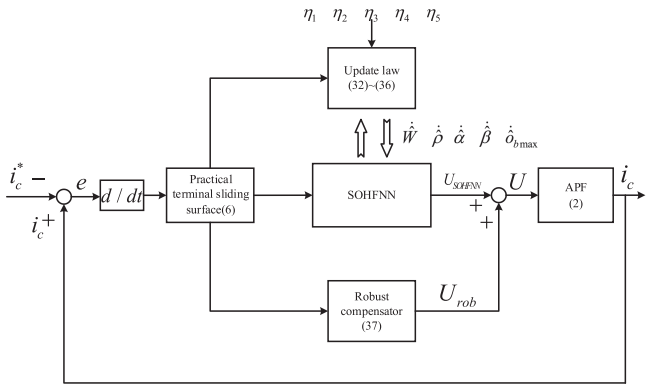

Fig. 3. Block diagram of STPTSMC based on SOHFNN for APF.

$$u_{rob} = -\hat{o}_{b\max}\mathrm{sgn}(s) \tag{37}$$

where $\tilde{o}_{b\max} = o^*_{b\max} - \hat{o}_{b\max}$. $\eta_i > 0, i = 1, \ldots, 5$.

The concluding control block diagram is illustrated in Fig. 3.

Proof: Selecting Lyapunov candidate function V_2 as:

$$V_2 = \frac{1}{2}s^2 + \frac{1}{2\eta_1}tr(\tilde{\rho}^T\tilde{\rho}^T) + \frac{1}{2\eta_2}tr(\tilde{\alpha}^T\alpha^T) + \frac{1}{2\eta_3}tr(\tilde{\beta}^T\beta^T) + \frac{1}{2\eta_4}tr\left(\tilde{W}^T\tilde{W}^T\right) + \frac{1}{2\eta_5}tr(\tilde{o}_{b\max}\tilde{o}_{b\max}) \tag{38}$$

where $tr()$represents the trace of a matrix, $\eta_i > 0, i = 1, \ldots, 5$.

Taking the derivative of V_2 to get

$$\dot{V}_2 = s\dot{s} + \frac{1}{\eta_1}tr(\tilde{\rho}^T\dot{\tilde{\rho}}^T) + \frac{1}{\eta_2}tr(\dot{\tilde{\alpha}}^T\alpha^T) + \frac{1}{\eta_3}tr\left(\dot{\tilde{\beta}}^T\beta^T\right) + \frac{1}{\eta_4}tr\left(\dot{\tilde{W}}^T\tilde{W}^T\right) + \frac{1}{\eta_5}tr(\dot{\tilde{o}}_{b\max}\tilde{o}_{b\max}). \tag{39}$$

When using a new controller, the derivative of the practical terminal sliding surface can be reorganized as

$$\dot{s} = H(t, i_c) - k_1\sqrt{|s|}\mathrm{sgn}(s) - s\int k_2\mathrm{sgn}(s)dt + u_{\mathrm{rob}} - \tilde{u}. \tag{40}$$

Substituting (31)–(37) into (39) to obtain

$$\dot{V}_2 = sH(t, i_c) - k_1|s|\sqrt{|s|} - s\int k_2\mathrm{sgn}(s)dt - |s|\hat{o}_{b\max} - s\cdot o_b - |s|\tilde{o}_{b\max}. \tag{41}$$

From (11)–(13), it can be derived that

$$\begin{aligned}\dot{V}_2 &\le -k_1|s|\sqrt{|s|} - |s|\hat{o}_{b\max} - s\cdot o_b - |s|\tilde{o}_{b\max}\\ &\le -k_1|s|\sqrt{|s|} - |s|\hat{o}_{b\max} + |s|o^*_{b\max} - |s|\tilde{o}_{b\max}\\ &= -k_1|s|\sqrt{|s|} + |s|(o^*_{b\max} - \tilde{o}_{b\max}) - |s|\hat{o}_{b\max}\\ &\le -k_1|s|\sqrt{|s|}\\ &\le 0.\end{aligned} \tag{42}$$

$\dot{V}_2$ is seminegative definite, indicating that system stability is assured. In addition, according to (42), it can be obtained that V_2 and s are bounded, then one can get that $\int_0^t |s|^{\frac{3}{2}}dt \le \frac{V_2(0)-V_2(t)}{k_1}$.

TABLE I
SYSTEM PARAMETERS

Parameter	Value
Grid voltage and frequency	$U_s = 24\,\mathrm{V}, f = 50\ \mathrm{Hz}$
Sample time	$10^{-5}\,s$
Capacitor on DC side	C=2200 μF, $U_{\mathrm{dc}} = 50$ V
	$L = 10\mathrm{mH}$, R=0.1 Ω
Nonlinear load	$R_{L1} = 5\,\Omega, R_{L2} = 15\,\Omega, C_L$=1 mF
Additional nonlinear load	$R_{AL1} = 15\,\Omega, R_{AL2} = 15\,\Omega, C_{AL}$=1 mF
IGBT Switching frequency	$f_{sw} = 20$ kHz

Since $V_2(0)$ is bounded and $V_2(t)$ is decreasing, $\lim_{t\to\infty}\int_0^t |s|^{\frac{3}{2}}dt$ is also bounded. According to Barbalat's lemma, it can be concluded that $\lim_{t\to\infty} s(t) = 0$, such that e and $\dot{e}$ will converge to zero. That is to say, starting from any initial value, compensation current can converge to reference current in front of uncertainties [51]. The convergence and robustness of the controller have been verified.

V. SIMULATION EVALUATION

This section evaluates the performance and benefits of the STPTSMC using SOHFNN for APF through simulations in MATLAB/Simulink. Specifications of APF are detailed in Table I. The setup for simulation parameters is carefully outlined, followed by the presentation of results and analyses under both steady-state and dynamic conditions. Comparative analyses further underscore the superior efficacy of this approach compared to traditional methods.

During the simulation, the parameters for the controller are specified as follows: $k = 100; \mu = 0.238; q = 3; p = 7$, $k_1 = 10$; and $k_2 = 300$. The initial parameters of the SOHFNN are set as $X = [i_c, \dot{i}_c, e]$, $m = 5$, $n = 3$, $T_{a\_1} = 0.1$, $T_{a\_2} = 0.2$, $T_{a\_3} = 10$, $T_{d\_1} = 0.1$, $T_{d\_2} = 0.2$, $T_{d\_3} = 4$, $a_T = 10$, $\varphi = [1, 1, 1, 1, 1]^T$, $\alpha = \mathbf{0} \in R^{5\times1}$, $\beta = \mathbf{1} \in R^{5\times1}$, and $\chi = 0.2$, the values of learning rates are designed as $\eta_1 = 10$, $\eta_2 = 10$, $\eta_3 = 10$, $\eta_4 = 100$, and $\eta_5 = 5000$.

Remark 3: The objective of APF is to modify the source current such that it becomes a sine wave synchronized with the sinusoidal source voltage [52]. To accomplish this goal, the reference compensation current i_c^* can be articulated as follows:

$$i_c^* = i_L - \gamma E_s\sin(\omega_s t) \tag{43}$$

where γ is a proper magnitude that regulates the amplitude of the source current, E_s and ω_s is the peak amplitude and angular frequency of the source voltage, respectively.

Remark 4: This article uses 24 V ac voltage and around 5 A current for experimental verification, mainly considering experimental safety, and debugging convenience. The low-voltage system reduces the safety risks of equipment debugging and operation, and facilitates repeated testing without high-voltage isolation conditions. Moreover, there still exist many low voltage scenarios including electric motor driven, industrial robot, LED

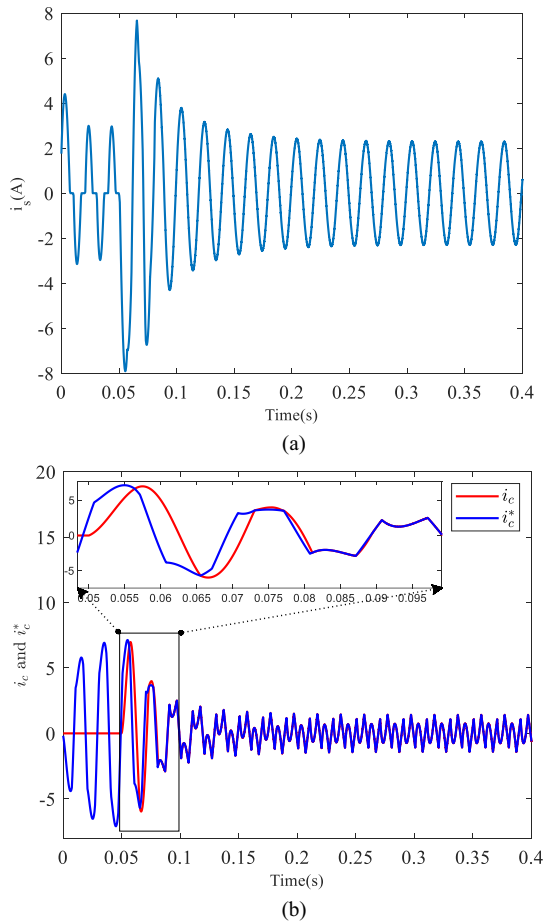

Fig. 4. Simulation waveform diagram using SOHFNN under steady-state. (a) i_s. (b) i_c and i_c^*.

lighting equipment, and other variable frequency system in real world, where the control requirements for THD are quite stringent. In addition, 10 mH inductor and 2200 μF capacitor is relatively large. However, this is mainly to provide a larger energy buffer and filtering margin to cope with the effects of switch voltage drop, measurement noise, etc., in the low-voltage system. According to the empirical formula [53], [54], the larger the compensating current is, the smaller the inductor value will be. In our future study, we will build a high-power platform with a smaller value of APF components.

A. Steady-State Simulation Results

Fig. 4 displays simulation waveform diagram using SOHFNN under steady-state, where APF is connected into grid at 0.05 s. It can be seen that i_s possesses severe distortions before compensation, and i_s can be purified into a clean sinusoidal shape after compensation by APF, where the developed SOHFNN imposes high-precision tracking between i_c and i_c^*.

In the design of APF controllers, total harmonic distortion (THD) is frequently utilized as a benchmark to evaluate the efficacy of various control strategies. A lower THD value is indicative of superior control performance. In Fig. 5, one can see

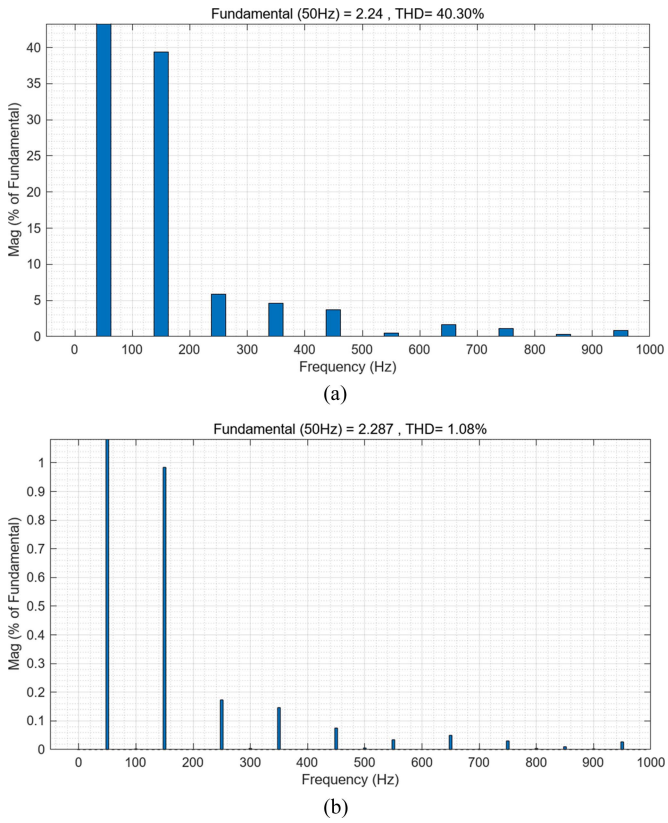

Fig. 5. Simulation spectrum analysis using SOHFNN under steady-state. (a) i_L. (b) i_s.

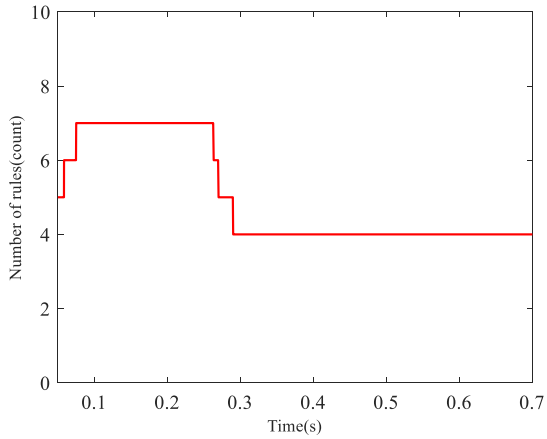

Fig. 6. Rule variation of SOHFNN.

that THD decreases from 40.30% to 1.08%, highlighting the deployed strategy's exceptional capability in harmonic reduction. Fig. 6 displays the rule variation of SOHFNN, where one can see the dynamic adjustment process of rule numbers, reflecting its capability to adaptively modify in response to demands.

B. Dynamic Simulation Results

This section will show how quickly the system stabilizes after a load change to further illustrate the controller's responsiveness. The additional load will be connected and disconnected at 0.35 and 0.7 s, respectively.

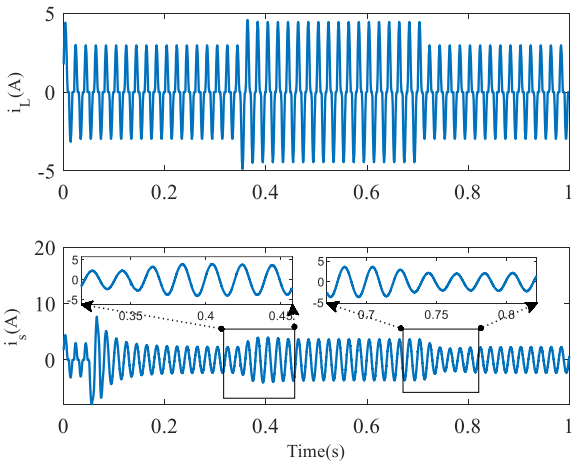

(a)

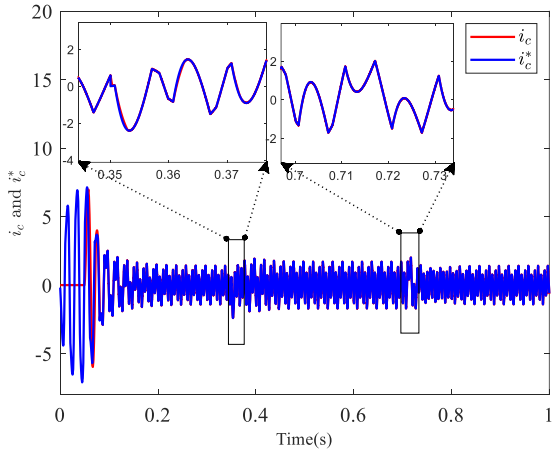

(b)

Fig. 7. Simulation spectrum analysis using SOHFNN under dynamic-state. (a) i_L and i_s. (b) i_c and i_c^*.

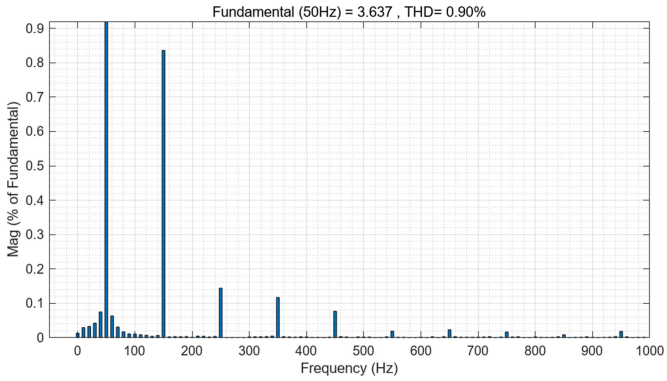

Fig. 8. Simulation spectrum analysis using SOHFNN under load increases.

As depicted in Fig. 7, the integration of an additional parallel nonlinear load results in an immediate surge in i_L. Despite this abrupt variation, the waveform of i_s still can be purified into a sinusoidal shape within just two cycles. Load decreased condition also reveals superior performance as shown in Fig. 7. Figs. 8 and 9 reveal that THD still can be maintained in an ideal level, demonstrating the efficacy and rapidity of the SOHFNN in adapting to dynamic load.

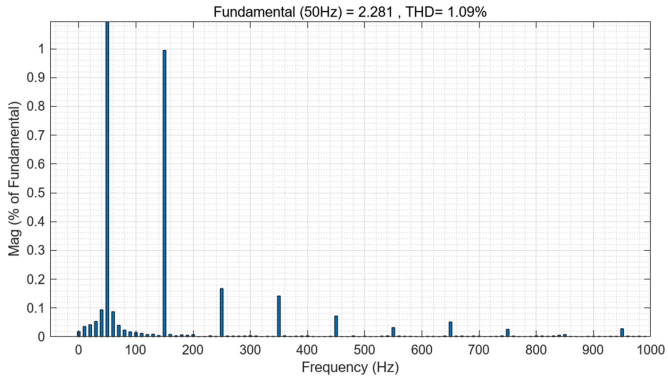

Fig. 9. Simulation spectrum analysis using SOHFNN under load decreases.

TABLE II
RESULTS OF PARAMETER PERTURBATION

AC inductance(mH)	DC capacitor(μF)	THD(%)
5	1100	2.42
5	1650	1.89
7.5	1100	2.20
7.5	1650	1.60

TABLE III
PERFORMANCE COMPARISON OF DIFFERENT METHODS

Method	THD (%)	RMSE	CT (s)	ET(s)
PI	2.00	1.3321	0.18939	14
fractional-order SMC	1.88	0.8740	0.08278	76
FNN	3.78	2.0456	0.15101	47
SOHFNN	1.08	0.0662	0.07834	98

To verify the anti-interference performance of the controller under fluctuations of system parameters, the ac inductance value and the dc-side capacitance value is set as 50% and 75% of the nominal value, respectively. The result data are given in Table II. It can be seen that although facing parameter disturbances, the THD still remains at a low level.

C. Comparison With Traditional Methods

To comprehensively compare the performance of SOHFNN with PI, fractional-order SMC, and FNN, the performance comparison results are collected in Table III. In addition to THD, three performance indicators including RMSE, convergence time (CT), and execution time (ET), have also been used to perform statistical analysis. It can be observed that the SOHFNN exhibits superior performance over its rivals. Though ET of SOHFNN is higher than other strategies, it is still an attractive solution with a detailed experimental validation in the following section.

Remark 5: In some high-precision and power-quality-sensitive practical scenarios, such as semiconductor manufacturing, precision instruments, aerospace systems, and medical

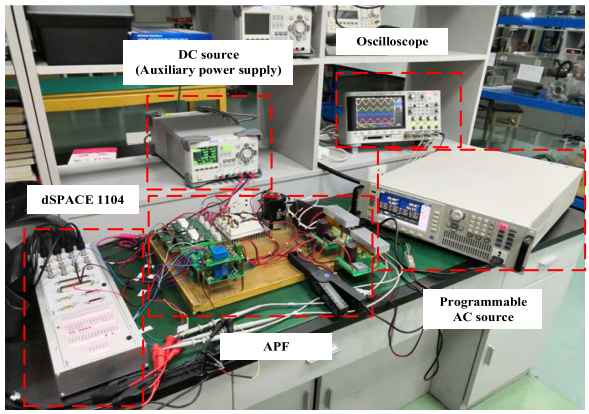

Fig. 10. Experimental platform.

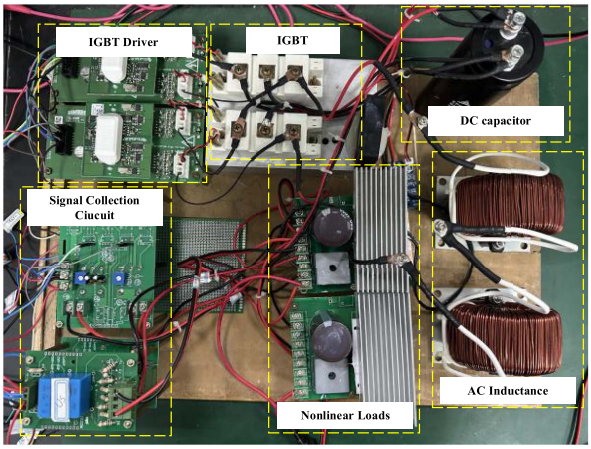

Fig. 11. Detailed APF main circuit module.

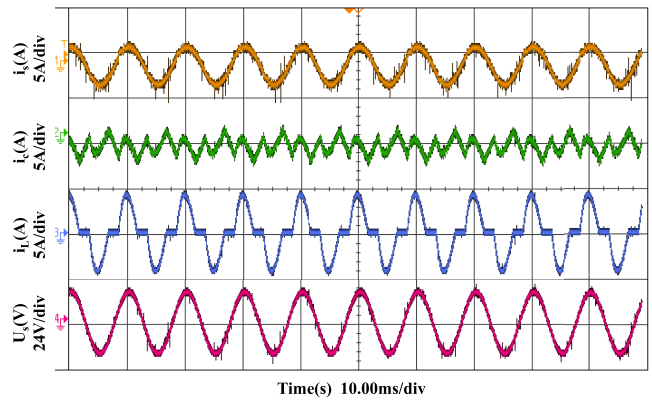

Fig. 12. Experimental waveform diagram using SOHFNN under steady-state.

equipment, the requirements for THD is to be as low as possible. In these applications, even minor harmonic may cause signal interference, performance degradation, or equipment malfunction. Therefore, controlling THD below 1.5% is of great significance to ensure the stability and safety of above-mentioned scenarios.

VI. Experimental Verification

The efficacy and reliability of the SOHFNN-STPTSMC model will be demonstrated through an experimental prototype.

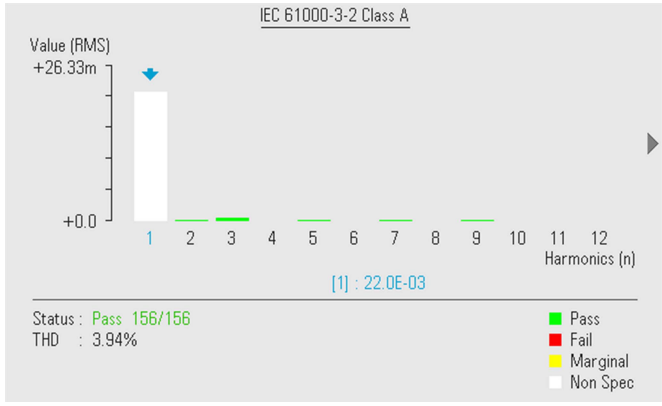

Fig. 13. Experimental spectrum analysis using SOHFNN under steady-state.

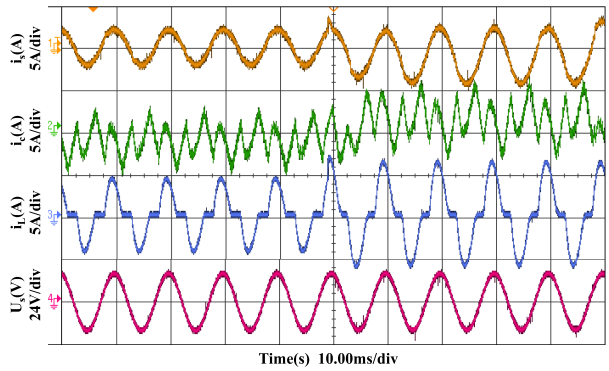

Fig. 14. Experimental waveform diagram using SOHFNN under load increases.

A. Structural Overview of the APF Prototype

Figs. 10 and 11 illustrate the architecture of the single-phase APF prototype, comprising a single-phase power supply, a nonlinear load, the APF module's main circuit, a signal collection module, an IGBT driver, and a dSPACE controller. The signal collection module is tasked with acquiring data regarding the dc-side capacitor voltage, power supply voltage, load current, and compensation current. This data enables the dSPACE controller to generate PWM signals through triangular carrier modulation, activating the IGBT switch to facilitate current compensation.

B. Steady-State Experimental Results

Figs. 12 and 13 present the steady-state experimental waveform diagram and its spectrum analysis. The waveform of i_L demonstrates notable distortion, and i_s with a smooth sinusoidal waveform, whose THD is reduced to 3.94%, are observed by implementing the SOHFNN-STPTSMC strategy. The experimental results demonstrate the strategy's effectiveness in minimizing harmonic components.

C. Dynamic Experimental Results

Similar with simulation verification, an additional load also is connected and disconnected to test dynamic performance, as shown in Figs. 14–17. Detailed dynamic response can be observed through these waveforms. It is noteworthy that THD

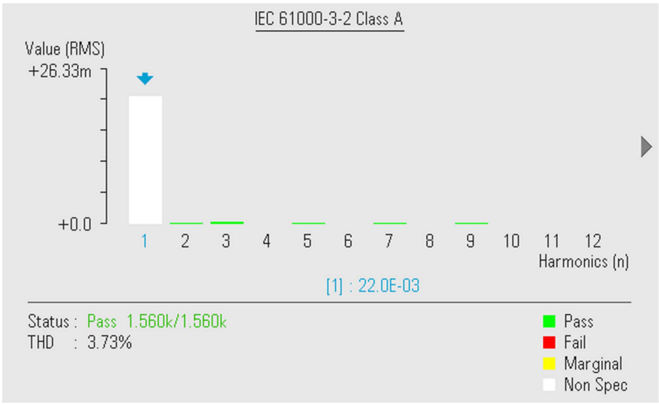

Fig. 15. Experimental spectrum analysis using SOHFNN under load increases.

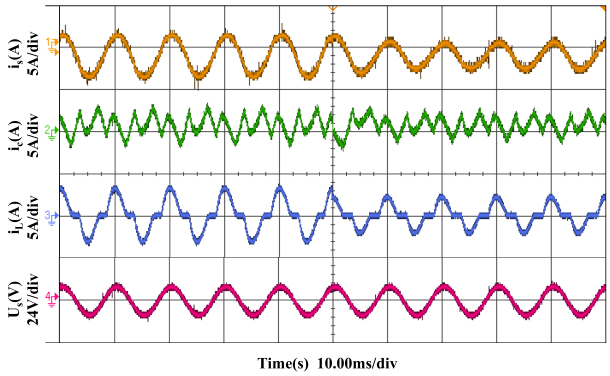

Fig. 16. Experimental waveform diagram using SOHFNN under load decreases.

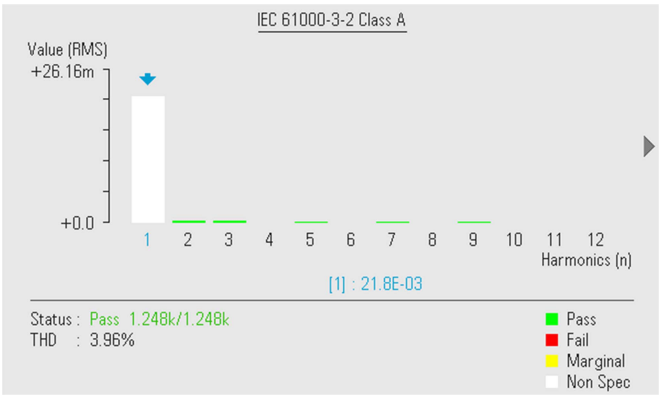

Fig. 17. Experimental spectrum analysis using SOHFNN under load decreases.

of i_s is 3.73% and 3.96%, respectively. Therefore, the proposed controller exhibits excellent harmonic compensation capabilities in both steady-state and dynamic scenarios.

D. Comparison With PI

In order to verify the effectiveness of the proposed method more comprehensively, the experimental results with the traditional PI control method are collected in Figs. 18–21. It is noteworthy that the THD is nearly 5%, which is close to

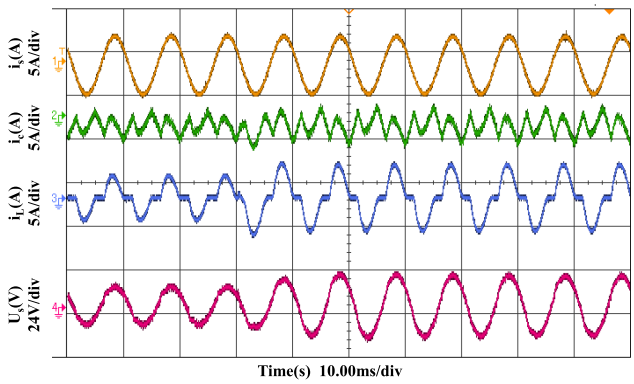

Fig. 18. Experimental waveform diagram using PI under load increases.

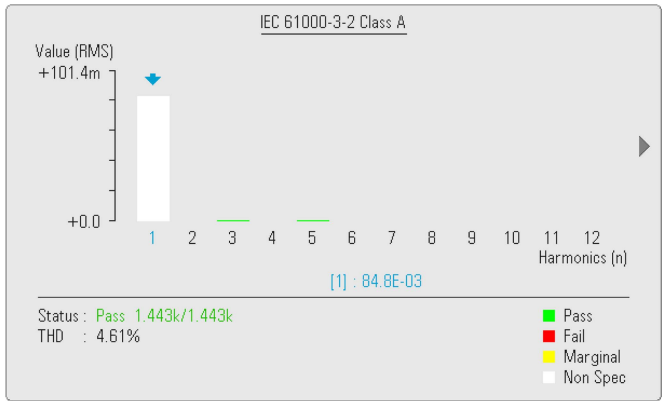

Fig. 19. Experimental spectrum analysis using PI under load increases.

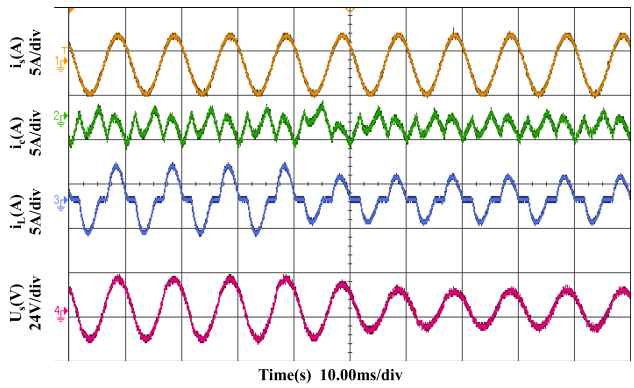

Fig. 20. Experimental waveform diagram using PI under load decreases.

the safety boundary, using PI under dynamic condition. In the same operation condition, the THD using the proposed scheme remains below 4%, further demonstrating the superior harmonic suppression performance of SOHFNN.

Remark 6: In recent years, the rapid development of very large-scale integration technology has significantly improved the computing power of microprocessors, making it entirely feasible to implement complex control strategies on high-performance DSPs [55], [56]. In addition, three-phase APF can be decoupled into three single-phase systems, then the

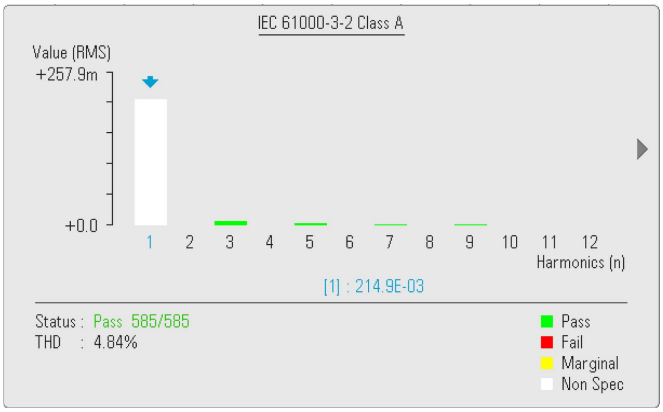

Fig. 21. Experimental spectrum analysis using PI under load decreases.

SOHFNN-STPTSMC control framework can independently optimize each phase, ensuring precise harmonic suppression.

VII. Conclusion

This article tackles the issue of APF current control amidst uncertainties, unveiling a strategy that utilizes Hermite orthogonal polynomials and a self-organizing mechanism, coupled with FS, to ensure enhanced control precision and system adaptability. By integrating Hermite orthogonal polynomials as the SOHFNN's activation function and implementing a self-organizing mechanism, the network's architecture is streamlined, concurrently augmenting its ability to express nonlinearities. The developed controller benefits from STPSTM's attributes, notably its resilience to disturbances and expedited convergence, ensuring compliance with stringent system control prerequisites. To address approximation inaccuracies, the design incorporates an adaptive robust compensator with an adaptive law. Empirical evidence underscores the technique's superiority, highlighted by its precision in steady states and agility in the dynamic response for harmonic current correction. Prospective research will investigate more efficacious evolutionary tactics and apply the formulated control scheme to diverse practical scenarios.

References

[1] Y. Pan, X. Sun, Y. Cai, X. Li, and W. Zhao, "An improved coordination control for enhancing photovoltaic power imbalance tolerant capability of MMC-based photovoltaic system," *IEEE Trans. Power Electron.*, vol. 39, no. 9, pp. 11732–11745, Sep. 2024, doi: 10.1109/TPEL.2024.3404398.

[2] M. Zhang, X. Sun, J. Teng, L. Qi, H. Shen, and X. Li, "Standing wave compensation-based harmonic propagation mitigation for closed-loop distribution feeder," *IEEE Trans. Power Electron.*, vol. 39, no. 11, pp. 14142–14147, Nov. 2024, doi: 10.1109/TPEL.2024.3432311.

[3] Y. Li, H. Yi, F. Zhuo, and X. Jiang, "Analysis and stabilization of APF systems considering dynamic of nonlinear loads," *IEEE Trans. Power Electron.*, vol. 39, no. 1, pp. 409–423, Jan. 2024, doi: 10.1109/TPEL.2023.3324650.

[4] H. Zhou, L. He, Z. Yang, and Z. Lin, "Virtual fractional-order-inductor based second harmonic current suppression method," *IEEE Trans. Ind. Electron.*, vol. 71, no. 8, pp. 8949–8959, Aug. 2024, doi: 10.1109/TIE.2023.3314915.

[5] P. Santiprapan, K. Areerak, and K. Areerak, "An adaptive gain of proportional-resonant controller for an active power filter," *IEEE Trans. Power Electron.*, vol. 39, no. 1, pp. 1433–1446, Jan. 2024, doi: 10.1109/TPEL.2023.3319476.

[6] S. Kim and P. N. Enjeti, "A new hybrid active power filter (APF) topology," *IEEE Trans. Power Electron.*, vol. 17, no. 1, pp. 48–54, Jan. 2002, doi: 10.1109/63.988669.

[7] E. S. Asl, E. Babaei, M. Sabahi, M. H. B. Nozadian, and C. Cecati, "New half-bridge and full-bridge topologies for a switched-boost inverter with continuous input current," *IEEE Trans. Ind. Electron.*, vol. 65, no. 4, pp. 3188–3197, Apr. 2018, doi: 10.1109/TIE.2017.2752118.

[8] L. Callegaro, M. Ciobotaru, D. J. Pagano, E. Turano, and J. E. Fletcher, "A simple smooth transition technique for the noninverting buck–Boost converter," *IEEE Trans. Power Electron.*, vol. 33, no. 6, pp. 4906–4915, Jun. 2018, doi: 10.1109/TPEL.2017.2731974.

[9] W.-H. Chen, S. Niu, and W. X. Zheng, "Sliding mode control with time-varying sliding surface for linear uncertain impulsive systems," *IEEE Trans. Autom. Control*, vol. 69, no. 7, pp. 4836–4843, Jul. 2024, doi: 10.1109/TAC.2024.3357756.

[10] B. Çavuş and M. Aktaş, "A new adaptive terminal sliding mode speed control in flux weakening region for DTC controlled induction motor drive," *IEEE Trans. Power Electron.*, vol. 39, no. 1, pp. 449–458, Jan. 2024, doi: 10.1109/TPEL.2023.3326383.

[11] Y. Chu, S. Fu, S. Hou, and J. Fei, "Intelligent terminal sliding mode control of active power filters by self-evolving emotional neural network," *IEEE Trans. Ind. Informat.*, vol. 19, no. 4, pp. 6138–6149, Apr. 2023, doi: 10.1109/TII.2022.3168654.

[12] T. Zhang, P. Shi, W. Li, and X. Yue, "Discrete nonsingular terminal sliding mode control for trajectory tracking of space manipulators with mismatched multiple disturbances and noisy measurements," *Aerosp. Sci. Technol.*, vol. 144, Jan. 2024, Art. no. 108766, doi: 10.1016/j.ast.2023.108766.

[13] H. Han, C. Feng, H. Sun, and J. Qiao, "Self-organizing fuzzy terminal sliding mode control for wastewater treatment processes," *IEEE Trans. Automat. Sci. Eng.*, vol. 21, no. 4, pp. 5421–5433, Oct. 2024, doi: 10.1109/TASE.2023.3311768.

[14] X. Sun et al., "Optimal design of terminal sliding mode controller for direct torque control of SRMs," *IEEE Trans. Transp. Electrific.*, vol. 8, no. 1, pp. 1445–1453, Mar. 2022, doi: 10.1109/TTE.2021.3111889.

[15] H. Dong, X. Yang, H. Gao, and X. Yu, "Practical terminal sliding-mode control and its applications in Servo systems," *IEEE Trans. Ind. Electron.*, vol. 70, no. 1, pp. 752–761, Jan. 2023, doi: 10.1109/TIE.2022.3152018.

[16] J. Yang, C. Yang, X. Zhang, and J. Na, "Fixed-time sliding mode control with varying exponent coefficient for modular reconfigurable flight arrays," *IEEE/CAA J. Automatica Sinica*, vol. 11, no. 2, pp. 514–528, Feb. 2024, doi: 10.1109/JAS.2023.123645.

[17] Q. Hou and S. Ding, "Finite-time extended State observer-based super-twisting sliding mode controller for PMSM drives with inertia identification," *IEEE Trans. Transp. Electrific.*, vol. 8, no. 2, pp. 1918–1929, Jun. 2022, doi: 10.1109/TTE.2021.3123646.

[18] H. Saied, A. Chemori, M. Bouri, M. E. Rafei, and C. Francis, "Feed-Forward super-twisting sliding mode control for robotic manipulators: Application to PKMs," *IEEE Trans. Robot.*, vol. 39, no. 4, pp. 3167–3184, Aug. 2023, doi: 10.1109/TRO.2023.3255586.

[19] M. Zhou, H. Su, Y. Feng, K. Wei, W. Xu, and J. Cheng, "Super-twisting algorithm-based fractional-order sliding-mode control of nonlinear systems with mismatched uncertainties," *IEEE Trans. Ind. Electron.*, vol. 71, no. 8, pp. 9510–9519, Aug. 2024, doi: 10.1109/TIE.2023.3329164.

[20] L. Chen et al., "Sensorless fixed-time sliding mode control of PMSM based on barrier function adaptive super-twisting observer," *IEEE Trans. Power Electron.*, vol. 39, no. 3, pp. 3037–3051, Mar. 2024, doi: 10.1109/TPEL.2023.3336743.

[21] D. Zhang, J. Hu, J. Cheng, Z.-G. Wu, and H. Yan, "A novel disturbance observer based fixed-time sliding mode control for robotic manipulators with global fast convergence," *IEEE/CAA J. Automatica Sinica*, vol. 11, no. 3, pp. 661–672, Mar. 2024, doi: 10.1109/JAS.2023.123948.

[22] P. Luo, Z. Yin, Z. Zhang, Y. Zhang, P. Zhang, and J. Liu, "Diversified diagnosis strategy for PMSM inter-turn short-circuit fault via novel sliding mode observer," *IEEE Trans. Power Electron.*, vol. 39, no. 4, pp. 4149–4159, Apr. 2024, doi: 10.1109/TPEL.2024.3352077.

[23] J. Wang and J. Fei, "Self-feedback neural network sliding mode control with extended state observer for active power filter," *IEEE Internet Things*, vol. 10, no. 13, pp. 11724–11738, Jul. 2023, doi: 10.1109/JIOT.2023.3242972.

[24] S. Hou, C. Wang, Y. Chu, and J. Fei, "Neural-observer-based terminal sliding mode control: Design and application," *IEEE Trans. Fuzzy Syst.*, vol. 30, no. 11, pp. 4800–4814, Nov. 2022, doi: 10.1109/TFUZZ.2022.3160614.

[25] U. Javaid, A. Mehmood, J. Iqbal, and A. A. Uppal, "Neural network and URED observer based fast terminal integral sliding mode control for energy efficient polymer electrolyte membrane fuel cell used in vehicular technologies," *Energy*, vol. 269, Apr. 2023, Art. no. 126717, doi: 10.1016/j.energy.2023.126717.
[26] Y. Wang and J. Zhao, "Neural-network-based event-triggered sliding mode control for networked switched linear systems with the unknown nonlinear disturbance," *IEEE Trans. Neural Netw. Learn. Syst.*, vol. 34, no. 8, pp. 3885–3896, Aug. 2023, doi: 10.1109/TNNLS.2021.3119665.
[27] Y. Qian, H. Zhang, and D. Hu, "Finite-time neural network-based hierarchical sliding mode antiswing control for underactuated dual ship-mounted cranes with unmatched sea wave disturbances suppression," *IEEE Trans. Neural Netw. Learn. Syst.*, vol. 35, no. 9, pp. 12396–12408, Sep. 2024, doi: 10.1109/TNNLS.2023.3257508.
[28] C. Yang, H. Pan, and J. Wang, "Convformer: Dual-stream vision transformers and convolutional networks for image restoration," *IEEE Trans. Instrum. Meas.*, vol. 73, 2024, Art. no. 2521410, doi: 10.1109/TIM.2024.3413168.
[29] X. Liu, H. Yan, W. Zhou, N. Wang, and Y. Wang, "Event-triggered optimal tracking control for underactuated surface vessels via neural reinforcement learning," *IEEE Trans. Ind. Informat.*, vol. 20, no. 11, pp. 12837–12847, Nov. 2024, doi: 10.1109/TII.2024.3424573.
[30] Y. Zhang et al., "Evolutionary game-based adaptive DT association and transfer for wireless computing power networks," *IEEE Trans. Green Commun. Netw.*, vol. 9, no. 2, pp. 670–683, Jun. 2025, doi: 10.1109/TGCN.2024.3442910.
[31] L. Ma and K. Khorasani, "Constructive feedforward neural networks using Hermite polynomial activation functions," *IEEE Trans. Neural Netw.*, vol. 16, no. 4, pp. 821–833, Jul. 2005, doi: 10.1109/TNN.2005.851786.
[32] J. Fei, L. Zhang, and Y. Fang, "Self-constructing Chebyshev fuzzy neural complementary sliding mode control and its application," *IEEE Trans. Neural Netw. Learn. Syst.*, vol. 36, no. 2, pp. 3084–3097, Feb. 2025, doi: 10.1109/TNNLS.2023.3347767.
[33] H. Wen, X. He, J. Xu, M. Zhou, and T. Huang, "Fixed-time neural networks with time-invariant and time-varying coefficients for mixed variational inequalities," *Inf. Sci.*, vol. 659, Feb. 2024, Art. no. 120078, doi: 10.1016/j.ins.2023.120078.
[34] A. Wang, L. Liu, J. Qiu, and G. Feng, "Leader-following consensus of multiple uncertain euler–Lagrange systems via fully distributed event-triggered adaptive fuzzy control," *IEEE Trans. Cybern.*, vol. 54, no. 1, pp. 76–86, Jan. 2024, doi: 10.1109/TCYB.2022.3177443.
[35] T. Yang, M. Zhai, Y. Fang, and N. Sun, "Adaptive fuzzy control of underactuated switched systems with disturbance observation and actuated/unactuated motion constraints," *IEEE Trans. Fuzzy Syst.*, vol. 32, no. 3, pp. 1195–1207, Mar. 2024, doi: 10.1109/TFUZZ.2023.3320145.
[36] G. Lai, K. Huang, Y. Wang, F. Wang, and H. Xiao, "Iterative inverse-based adaptive fuzzy control with predetermined tracking accuracy for hysteretic nonlinear systems," *IEEE Trans. Fuzzy Syst.*, vol. 32, no. 4, pp. 2509–2522, Apr. 2024, doi: 10.1109/TFUZZ.2023.3349268.
[37] G. Xue, Q. Chang, J. Wang, K. Zhang, and N. R. Pal, "An adaptive neuro-fuzzy system with integrated feature selection and rule extraction for high-dimensional classification problems," *IEEE Trans. Fuzzy Syst.*, vol. 31, no. 7, pp. 2167–2181, Jul. 2023, doi: 10.1109/TFUZZ.2022.3220950.
[38] J. Wang, H. Li, H. Yang, and Y. Wang, "Intelligent multivariable air-quality forecasting system based on feature selection and modified evolving interval type-2 quantum fuzzy neural network," *Environ. Pollut.*, vol. 274, Apr. 2021, Art. no. 116429, doi: 10.1016/j.envpol.2021.116429.
[39] F.-J. Lin, K.-H. Tan, Y.-K. Lai, and W.-C. Luo, "Intelligent PV power system with unbalanced current compensation using CFNN-AMF," *IEEE Trans. Power Electron.*, vol. 34, no. 9, pp. 8588–8598, Sep. 2019, doi: 10.1109/TPEL.2018.2888732.
[40] H. Han, H. Liu, and J. Qiao, "Data-knowledge-driven self-organizing fuzzy neural network," *IEEE Trans. Neural Netw. Learn. Syst.*, vol. 35, no. 2, pp. 2081–2093, Feb. 2024, doi: 10.1109/TNNLS.2022.3186671.
[41] K. Zhou, S.-K. Oh, J. Qiu, W. Pedrycz, K. Seo, and J. H. Yoon, "Design of hierarchical neural networks using deep LSTM and self-organizing dynamical fuzzy-neural network architecture," *IEEE Trans. Fuzzy Syst.*, vol. 32, no. 5, pp. 2915–2929, May 2024, doi: 10.1109/TFUZZ.2024.3361856.
[42] H.-G. Han, C.-C. Feng, H.-Y. Sun, and J.-F. Qiao, "Hierarchical self-organizing fuzzy control for uncertain nonlinear systems," *IEEE Trans. Fuzzy Syst.*, vol. 32, no. 4, pp. 2471–2482, Apr. 2024, doi: 10.1109/TFUZZ.2024.3351673.
[43] M. Yang, Y. Guo, S. Zhu, N. Tan, B. Liao, and H. Zhang, "A novel data-driven DRNN-SMC model for redundant manipulators," *IEEE Trans. Syst., Man, Cybern., Syst.*, vol. 55, no. 6, pp. 4322–4333, Jun. 2025, doi: 10.1109/TSMC.2025.3550943.
[44] H. Wang et al., "A cascade PI-SMC method for matrix converter-fed BD-FIM drives," *IEEE Trans. Transp. Electrific.*, vol. 7, no. 4, pp. 2541–2550, Dec. 2021, doi: 10.1109/TTE.2021.3061742.
[45] A. M. Patrikar, "Approximating Gaussian mixture model or radial basis function network with multilayer perceptron," *IEEE Trans. Neural Netw. Learn. Syst.*, vol. 24, no. 7, pp. 1161–1166, Jul. 2013, doi: 10.1109/TNNLS.2013.2249086.
[46] Y. He, L. Xiao, Z. Wang, Q. Zuo, and L. Li, "A fuzzy neural network approach to adaptive robust nonsingular sliding mode control for predefined-time tracking of a quadrotor," *IEEE Trans. Fuzzy Syst.*, vol. 32, no. 12, pp. 6775–6788, Dec. 2024, doi: 10.1109/TFUZZ.2024.3464564.
[47] Y. Zhang, B. Niu, X. Zhao, P. Duan, H. Wang, and B. Gao, "Global predefined-time adaptive neural network control for disturbed pure-feedback nonlinear systems with zero tracking error," *IEEE Trans. Neural Netw. Learn. Syst.*, vol. 34, no. 9, pp. 6328–6338, Sep. 2023, doi: 10.1109/TNNLS.2021.3135582.
[48] W. Dai, L. Zhang, J. Fu, T. Chai, and X. Ma, "Dual-rate adaptive optimal tracking control for dense medium separation process using neural networks," *IEEE Trans. Neural Netw. Learn. Syst.*, vol. 32, no. 9, pp. 4202–4216, Sep. 2021, doi: 10.1109/TNNLS.2020.3017184.
[49] H. Wang et al., "Continuous fast nonsingular terminal sliding mode control of automotive electronic throttle systems using finite-time exact observer," *IEEE Trans. Ind. Electron.*, vol. 65, no. 9, pp. 7160–7172, Sep. 2018, doi: 10.1109/TIE.2018.2795591.
[50] K. Shao, J. Zheng, H. Wang, F. Xu, X. Wang, and B. Liang, "Recursive sliding mode control with adaptive disturbance observer for a linear motor positioner," *Mech. Syst. Signal Proc.*, vol. 146, Jan. 2021, Art. no. 107014, doi: 10.1016/j.ymssp.2020.107014.
[51] L. Xiao, S. Li, F.-J. Lin, Z. Tan, and A. H. Khan, "Zeroing neural dynamics for control design: Comprehensive analysis on stability, robustness, and convergence speed," *IEEE Trans. Ind. Informat.*, vol. 15, no. 5, pp. 2605–2616, May 2019, doi: 10.1109/TII.2018.2867169.
[52] S. Echalih et al., "Nonlinear control design and stability analysis of single phase half bridge interleaved buck shunt active power filter," *IEEE Trans. Circuits Syst. I: Reg. Papers*, vol. 69, no. 5, pp. 2117–2128, May 2022.
[53] S. K. Khadem, M. Basu, and M. F. Conlon, "Harmonic power compensation capacity of shunt active power filter and its relationship with design parameters," *Int. Eng. Technol. Power Electron.*, vol. 7, pp. 418–430, 2014, doi: 10.1049/iet-pel.2013.0098.
[54] Z. Wang et al., *Harmonic Suppression and Reactive Power Compensation*. China: Mach. Press, 2005, pp. 280–284.
[55] W. Zhou et al., "Comparison of real- and complex-valued NN equalizers for photonics-aided 90-Gbps D-band PAM-4 coherent detection," *J. Lightw. Technol.*, vol. 39, no. 21, pp. 6858–6868, Nov. 2021, doi: 10.1109/JLT.2021.3109126.
[56] Q. Fan, C. Lu, and A. P. T. Lau, "Combined neural network and adaptive DSP training for long-haul optical communications," *J. Lightw. Technol.*, vol. 39, no. 22, pp. 7083–7091, Nov. 2021, doi: 10.1109/JLT.2021.3111437.

Shixi Hou received the B.S. degree in automation and the Ph.D. degree in electrical engineering from Hohai University, Nanjing, China, in 2011 and 2016, respectively.

He is currently an Associate Professor with Hohai University. His research interests include power electronics, adaptive control, nonlinear control, and intelligent control.

Jienan Han received the B.S. degree in automation in 2023 from Hohai University, Nanjing, China, where she is currently working toward the M.S. degree in control engineering.

Her research interests include adaptive control, sliding mode control, nonlinear control, intelligent control.

Yundi Chu received the B. S., M.S., and Ph.D. degrees in electrical engineering from Hohai University, Nanjing, China, in 2013, 2016, and 2019, respectively.

She is currently an Associate Professor with Hohai University. Her research interests include power electronics, adaptive control, intelligent control, nonlinear control etc.

Cheng Zhou received the B.S. degree in automation in 2022 from Hohai University, Nanjing, China, where he is currently working toward the M.S. degree in control engineering.

His research interests include adaptive control, sliding mode control, nonlinear control, intelligent control.

Juntao Fei (Senior Member, IEEE) received the B.S. degree in electrical engineering from Hefei University of Technology, Hefei, China in 1991, the M.S. degree in electrical engineering from the University of Science and Technology of China, Hefei, China, in 1998, and the M.S. and Ph.D. degrees in mechanical engineering from The University of Akron, OH, USA in 2003 and 2007, respectively.

He was a Visiting Scholar with University of Virginia, Charlottesville, VA, USA, during 2002–2003. He was a Postdoctoral Research Fellow and an Assistant Professor with the University of Louisiana, Lafayette, LA, USA, from 2007 to 2009. He is currently a Professor with Hohai University, Nanjing, China. His research interests include adaptive control, nonlinear control, intelligent control, dynamics and control of MEMS, and smart materials and structures.